

Effects of elastic focusing on global models of Rayleigh wave attenuation

Xueyang Bao,^{1,*} Colleen A. Dalton¹ and Jeroen Ritsema²

¹*Earth, Environmental and Planetary Sciences, Brown University, 324 Brook Street, Providence, RI 02912, USA. E-mail: xybao@uri.edu*

²*Geological Sciences, University of Michigan, 1100 North University Avenue, Ann Arbor, MI 48109, USA*

Accepted 2016 August 24. Received 2016 July 25; in original form 2015 November 20

SUMMARY

Rayleigh wave amplitudes are the primary data set used for imaging shear attenuation in the upper mantle on a global scale. In addition to attenuation, surface-wave amplitudes are influenced by excitation at the earthquake source, focusing and scattering by elastic heterogeneity, and local structure at the receiver and the instrument response. The challenge of isolating the signal of attenuation from these other effects limits both the resolution of global attenuation models and the level of consistency between different global attenuation studies. While the source and receiver terms can be estimated using relatively simple approaches, focusing effects on amplitude are a large component of the amplitude signal and are sensitive to multiscale velocity anomalies. In this study we investigate how different theoretical treatments for focusing effects on Rayleigh wave amplitude influence the retrieved attenuation models. A new data set of fundamental-mode Rayleigh wave phase and amplitude at periods of 50 and 100 s is analysed. The amplitudes due to focusing effects are predicted using the great-circle ray approximation (GCRA), exact ray theory (ERT), and finite-frequency theory (FFT). Phase-velocity maps expanded to spherical-harmonic degree 20 and degree 40 are used for the predictions. After correction for focusing effects, the amplitude data are inverted for global attenuation maps and frequency-dependent source and receiver correction factors. The degree-12 attenuation maps, based on different corrections for focusing effects, all contain the same large-scale features, though the magnitude of the attenuation variations depends on the focusing correction. The variance reduction of the amplitudes strongly depends on the predicted focusing amplitudes, with the highest variance reduction for the ray-based approaches at 50 s and for FFT at 100 s. Although failure to account for focusing effects introduces artefacts into the attenuation models at higher spherical-harmonic degrees, the low-degree structure can be robustly retrieved. The new attenuation maps compare favourably with previous attenuation studies derived using independent amplitude data sets.

Key words: Surface waves and free oscillations; Seismic attenuation; Seismic tomography; Theoretical seismology.

1 INTRODUCTION

It is generally acknowledged that better constraints on seismic attenuation in Earth's mantle would be valuable. As has been pointed out by numerous earlier studies, seismic attenuation provides a direct measure of Earth's anelastic properties and, as such, allows more definite conclusions to be drawn about mantle temperature, composition, melt content, and volatile content than is possible from seismic velocity alone (e.g. Romanowicz 1995; Roth *et al.* 2000;

Cooper 2002; Jackson *et al.* 2002; Gung & Romanowicz 2004; Faul & Jackson 2005; Yang *et al.* 2007; Rychert *et al.* 2008; Dalton & Faul 2010; Abers *et al.* 2014). Furthermore, anelasticity causes a frequency dependence of seismic velocity, and constraints on attenuation are needed to separate the frequency-independent elastic and frequency-dependent anelastic components of wave speed, resulting in an improved interpretation of velocity anomalies (e.g. Liu *et al.* 1976; Karato 1993; Lekić *et al.* 2009).

Surface-wave amplitudes are the primary data set for measuring seismic attenuation in the upper mantle on a global scale. The amplitudes' sensitivity to factors in addition to attenuation, including source excitation, focusing/defocusing and scattering by elastic heterogeneity, and site amplification and the instrument response

*Now at: Graduate School of Oceanography, University of Rhode Island, 215 South Ferry Road, Narragansett, RI 02882, USA.

at the receiver, make it difficult to isolate the signal of attenuation in the amplitudes. For this reason, global shear-attenuation models (e.g. Romanowicz 1995; Bhattacharyya *et al.* 1996; Reid *et al.* 2001; Selby & Woodhouse 2002; Gung & Romanowicz 2004; Dalton *et al.* 2008) have not yet achieved the same level of consistency and lateral resolution that global shear-velocity models have (e.g. Kustowski *et al.* 2008; Ritsema *et al.* 2011; Schaeffer & Lebedev 2013; French & Romanowicz 2014).

In this paper, we investigate how the treatment of elastic focusing effects influences the features of attenuation models obtained by inverting a global data set of Rayleigh wave amplitudes. Indeed, the signal due to focusing effects is the main obstacle for both global and regional surface-wave attenuation studies. Previous studies have noted that source excitation has a non-negligible effect on Rayleigh wave amplitudes (Dalton & Ekström 2006a, hereinafter DE06; Ferreira & Woodhouse 2007; Dalton *et al.* 2014; Ma *et al.* 2016). However, when an event has been recorded by numerous stations, the average amplitude anomaly for each event can be considered a useful correction for the effects of source-excitation uncertainties on amplitudes (Dalton *et al.* 2014). This approach is especially valuable if the assumed local structure at the earthquake location is in error, as that effect is largely independent of azimuth. It is less effective if, for example, there are large uncertainties in the assumed radiation pattern, as that effect will depend on azimuth. Similarly, both the average amplitude recorded by each receiver for a large number of events and the average phase velocity at the receiver can be used to approximate the effect of local structure at the receiver location on amplitude (Dalton & Ekström 2006b; Dalton *et al.* 2014; Ma *et al.* 2016).

Focusing effects on amplitude depend on the phase-velocity gradient perpendicular to the propagation path, causing the amplitudes to be sensitive to the wavelength of elastic heterogeneity and to errors in the assumed propagation path. Here, we consider three theoretical approximations for surface-wave propagation: the great-circle ray approximation (GCRA), exact/JWKB ray theory (ERT), and finite-frequency theory (FFT). We also consider relatively smooth (spherical-harmonic degree 20) and rough (degree 40) elastic earth models. For each path in our amplitude data set, focusing effects are predicted using each approximate theory and phase-velocity map expansion, resulting in six sets of predicted focusing amplitudes. Previous comparisons of predicted focusing amplitudes have demonstrated that (Wang & Dahlen 1994; Wang & Dahlen 1995; Larson *et al.* 1998; Dalton *et al.* 2014): (1) Ray-based approaches (GCRA and ERT) are most useful if elastic heterogeneity is smooth and of a length scale larger than the seismic-wave wavelength. As period and seismic-wave wavelength increase, model roughness must be reduced for this condition to be met. Otherwise, the finite-frequency sensitivity of the surface wave must be considered. (2) Approximating the ray path as the great-circle path rather than the exact ray path is most appropriate for phase delays along short paths and less appropriate for longer paths and for amplitudes. (3) Approximating the surface-wave sensitivity zone as a thin ray works best for phase delays accumulated along short paths. We note, however, that Dalton & Ekström (2006b) showed that Rayleigh wave phase-velocity maps, expanded to spherical-harmonic degree 20, could be successfully obtained by inverting amplitude observations alone (i.e. no traveltimes observations) using GCRA, indicating that GCRA can be useful for Rayleigh wave focusing effects calculated in relatively smooth Earth models.

Recently, Dalton *et al.* (2014) used synthetic seismograms calculated with the spectral element method to evaluate the different approximate theories for focusing effects. They prescribed a 3-D

elastic model and a 1-D anelastic model and, after removing source and receiver effects on the fundamental-mode Rayleigh wave amplitudes, attributed the remaining signal to focusing effects. Through comparison with the predicted focusing amplitudes they showed that at shorter periods (50 s) ERT provided the best representation of focusing effects and at longer periods FFT did. At all periods GCRA provided the weakest agreement, especially when a relatively rough elastic model was used as input. These results indicated that for the shorter-period (shorter-wavelength) Rayleigh waves it is more important to allow for ray bending than to allow for the width of the sensitivity zone surrounding the great-circle path, whereas for the longer-period (longer-wavelength) waves including the sensitivity zone is more important than allowing for ray bending. Dalton *et al.* (2014) also showed that failure to remove focusing effects from amplitudes introduced artefacts into attenuation models at higher spherical-harmonic degrees, but the lower degrees (i.e. degrees < 6) of anelastic models can be faithfully recovered.

This paper is concerned with the effects of elastic focusing on surface-wave amplitudes and on our ability to recover anelastic structure in the real Earth. We use a large global data set of fundamental-mode Rayleigh wave phase and amplitude measured using the approach of van Heijst & Woodhouse (1997). This amplitude data set has not previously been used, and we first compare it to a separate amplitude data set measured using the approach of Ekström *et al.* (1997). The effect of focusing on amplitudes is predicted for GCRA, ERT and FFT using smooth and rough phase-velocity maps. We investigate the extent to which these predicted focusing amplitudes influence the features in our attenuation maps. Through calculation of variance reduction we also evaluate the three approximate theories and whether the findings of Dalton *et al.* (2014) using synthetic waveforms apply to Rayleigh wave propagation through the real Earth.

2 DATA

We utilize Rayleigh wave phase and amplitude observations measured using the Mode Branch Stripping technique of van Heijst & Woodhouse (1997). Surface-wave eigenfrequency measurements obtained with this approach have been used in many previous studies (e.g. Van Heijst & Woodhouse 1999; Trampert & van Heijst 2002; Ritsema *et al.* 2004, 2011); this study represents the first application of the amplitude data set. While we primarily focus on the fundamental-mode Rayleigh wave amplitudes, the fundamental-mode phase measurements are also utilized to derive phase-velocity maps that are needed for calculations of focusing effects. Path-averaged phase velocity perturbations $\delta c/c$ are determined from the path-averaged eigenfrequency perturbations $\delta\omega/\omega$ using the relation $\delta c/c = (c/U)\delta\omega/\omega$ (e.g. Dahlen & Tromp 1998), where c and U are the reference phase and group velocity, respectively. The original data set, which includes 1 090 418 amplitude and phase measurements at 50 s and 900 336 measurements at 100 s (Table S1), is derived from 12 121 earthquakes with $M_w > 5.0$ that occurred between 1991 and 2007 recorded at 1461 permanent and temporary broadband seismic stations. We consider minor-arc paths with epicentral distances in the range 30° – 160° and periods of 50 and 100 s in this study.

We compare the measurements used in this study to two previous data sets for 204 002 paths in common. Those two data sets are (1) the phase-anomaly data obtained using the approach of Ekström *et al.* (1997) and used by Ekström (2011) to generate the Global Dispersion Model GDM52 and (2) the amplitude data set

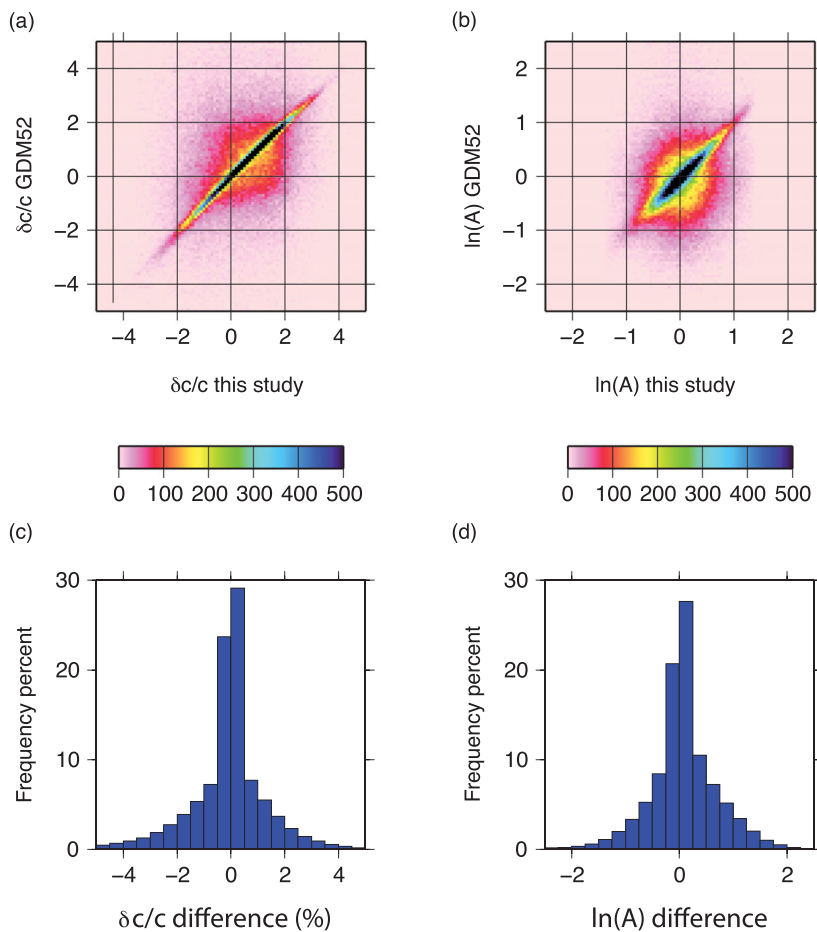


Figure 1. Comparison of our fundamental-mode Rayleigh wave phase and amplitude measurements at 50 s with two previous data sets. There are 204 002 common paths among the three data sets. (a) A 2-D histogram resulting from comparison of path-averaged phase velocity perturbations of the data set used to generate the Global Dispersion Model GDM52 (Ekström 2011) and our data set. (b) A 2-D histogram resulting from comparison of relative amplitude $\ln A$ used to generate the global attenuation model QRFSI12 (Dalton *et al.* 2008) and our data. (c) Distribution of the difference in $\delta c/c$ values from (a). (d) Distribution of the difference in $\ln A$ values from (b).

measured with the approach of Ekström *et al.* (1997), which was used by Dalton *et al.* (2008) to generate the global attenuation model QRFSI12. Fig. 1(a) shows the comparison for the overlapping $\delta c/c$ data sets of this study and of Ekström (2011). The absolute value of the difference between the two sets of path-averaged $\delta c/c$ values is <1 per cent for 66 per cent of all paths considered, and <2 per cent for 85 per cent of all paths (Fig. 1c). In Fig. 1(b), which shows the comparison of logarithmic amplitudes from this study and from Dalton *et al.* (2008), the absolute value of the difference between the two sets of path-averaged $\ln A$ values is <0.5 for 67 per cent of all paths considered and <1 for 88 per cent of all paths (Fig. 1d).

Several selection criteria are applied to the original phase velocity and amplitude data sets. First, the entire data set of path-averaged phase-velocity perturbations is used to generate 2-D phase-velocity maps at each period, expanded in spherical harmonics to degree 20, using the relation

$$\frac{\overline{\delta c_{ij}}}{c_0}(\omega) = \sum_{l=0}^{L_c} \sum_{m=-l}^l C_{lm}(\omega) \overline{Y_{lm}^{ij}}, \quad (1)$$

where L_c is the maximum degree of the expansion, C_{lm} are the coefficients to be solved, ω is the angular frequency and $\overline{Y_{lm}^{ij}}$ is the path average of the spherical-harmonic function Y_{lm} along the great-circle path connecting the earthquake i and station j . This method contains the assumption of surface-wave propagation along a great-

circle ray path; Ritsema *et al.* (2011) have shown that differences between Rayleigh wave phase-velocity maps determined with GCRA and with FFT are smaller than differences that can be achieved by variable amounts of damping. From these initial phase-velocity maps path-averaged phase velocity is predicted for all paths in our data set by integration along the great-circle ray path, and comparison of the observed and predicted values is used to identify outliers. We discard the measurements with the relative difference between observed and predicted path-averaged phase velocity perturbations $\delta c/c$ greater than 1 per cent, which approximately corresponds to removing values outside of two standard deviations of the mean. This step removes 74 768 paths at 50 s and 20 409 paths at 100 s. The final phase-velocity maps (Fig. 2) are obtained through inversion of this selected data set, which includes 1 015 650 paths from 11 310 earthquakes and 1240 stations at 50 s, and 879 927 paths from 10 874 earthquakes and 1240 stations at 100 s (Table S1). The data selection improves variance reduction by approximately 5 per cent and does not cause significant changes in the features of the tomographic maps: The correlation coefficients between the spherical-harmonic degree-20 phase-velocity maps from unselected and selected paths are 0.97 and 0.98 for 50 and 100 s, respectively.

Three additional selection criteria are applied to the amplitude data set. One, we remove observations with data-quality values, which are assigned during the measurement procedure, larger than 10.0. The choice of 10.0 as the data-quality criterion is arrived at

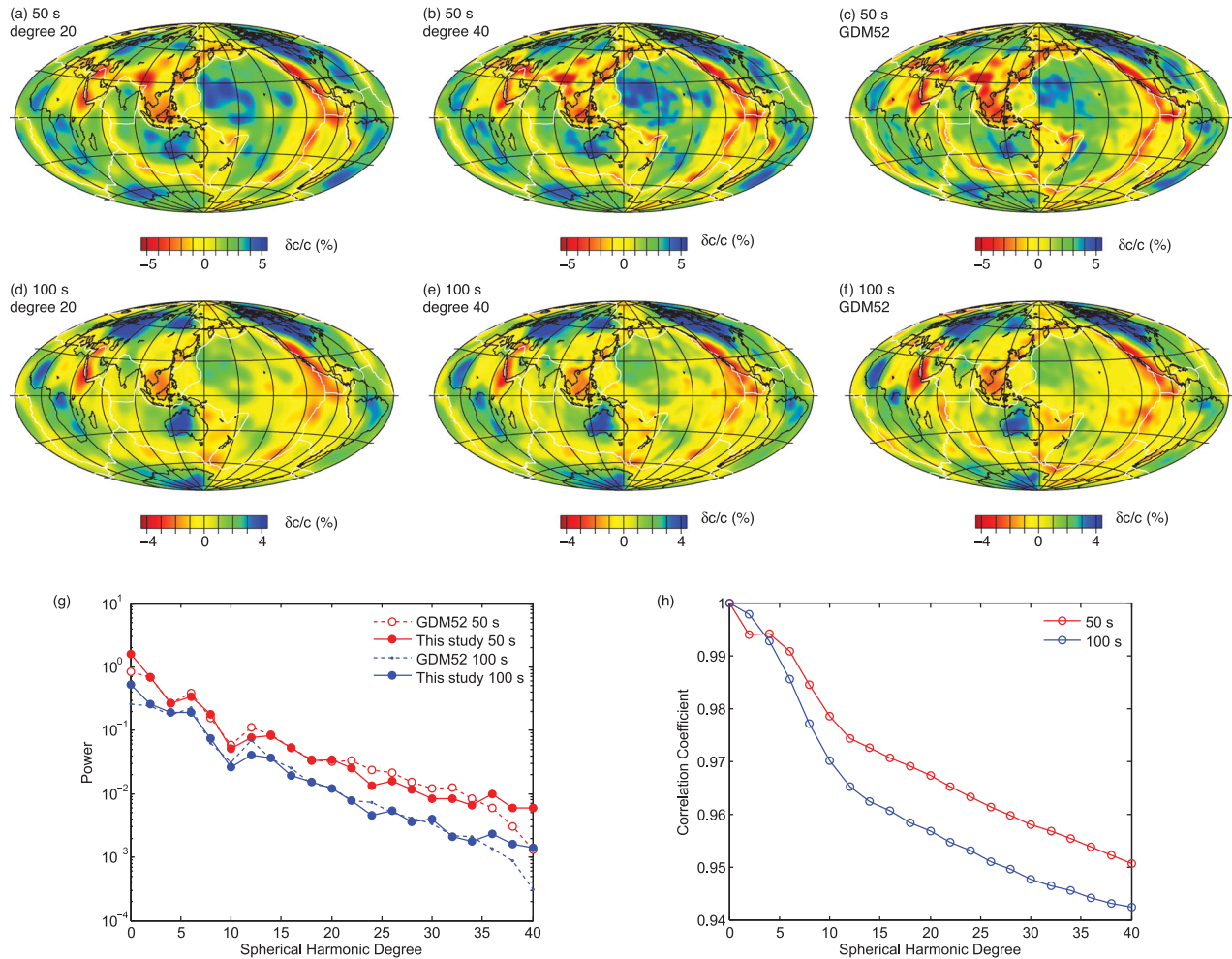


Figure 2. (a–b, d–e) Rayleigh wave phase-velocity maps, obtained by inverting the path-averaged $\delta c/c$ c measurements, expanded to spherical-harmonic degree 20 and 40 for 50 s (a–b) and 100 s (d–e). The degree-20 maps are generated by truncating the degree-40 maps. (c and f) GDM52 phase-velocity maps (Ekström 2011) expanded to spherical-harmonic degree 50. (g) The power spectra of the phase-velocity maps. (h) Cumulative correlation coefficient between our phase-velocity maps and GDM52 for 50 and 100 s.

through comparison with the quality values reported for the amplitude data set utilized by Dalton *et al.* (2008), with which we have extensive experience. Two, paths with their source-radiation amplitude < 50 per cent of the maximum value for the corresponding event are discarded. Dalton *et al.* (2014) and Ma *et al.* (2016) have shown that removing Rayleigh wave paths near a node in the radiation pattern reduces the scatter in the data set. Source-radiation amplitude is predicted using the Global CMT moment-tensor solutions (e.g. Ekström *et al.* 2012). Finally, we follow DE06 and require that each earthquake and station has at least 30 measurements associated with it at each period. Earthquakes and stations with fewer than 30 associated paths are removed. The final amplitude data set contains 390 360 paths from 4621 earthquakes and 1132 stations at 50 s and 393 464 paths from 4092 earthquakes and 1159 stations at 100 s.

3 METHOD

Each surface-wave amplitude measurement A_{ij} , generated by earthquake i and recorded by station j , at angular frequency ω is considered to be a product of four terms

$$A_{ij}(\omega) = A_i^S(\omega) A_j^R(\omega) A_{ij}^F(\omega) A_{ij}^Q(\omega), \quad (2)$$

where the superscripts S , R , F and Q represent contributions from the source, receiver, focusing and defocusing effects, and anelastic attenuation, respectively. In this study, the amplitude is measured with respect to the corresponding amplitude in a reference synthetic seismogram. The reference waveform is generated by mode summation using event parameters from the Global Centroid Moment Tensor (GCMT) catalogue (Ekström *et al.* 2012), the reported instrument response of each seismic station, and 1-D Earth structure from PREM (Dziewonski & Anderson 1981). Thus, amplitude values not equal to unity indicate that the source, receiver, focusing, and/or attenuation parameters assumed for the calculation of the synthetic seismogram require adjustment. Differences between the observed and reference waveforms could be due to: (1) the calculation of source excitation, including uncertainties in the CMT solution and assumptions about the local Earth structure at the centroid location or source duration; (2) the calculation of receiver amplitude, including local Earth structure at the receiver location and inaccuracies in the reported instrument response; (3) focusing and defocusing by elastic heterogeneity, which is absent in the synthetic waveform and (4) imperfect amplitude measurements, for example because of interference of overtones with the fundamental mode.

In this study, we are interested in how different theoretical and practical treatments of focusing effects on surface-wave amplitude influence the retrieved attenuation structure. We calculate focusing effects on amplitude for six scenarios, using three different theoretical approximations and two sets of phase-velocity maps, as described below. While source (A_i^S) and receiver (A_j^R) effects can have a measurable and non-negligible impact on amplitude (e.g. Ferreira & Woodhouse 2007), Dalton *et al.* (2014) have shown that the source term can be accurately estimated by calculating the average amplitude recorded by all stations for each event and the receiver term can be estimated as the average amplitude of all events recorded by each station. We follow the same procedure here.

The effect of attenuation on wave amplitude is expressed as

$$A_{ij}^Q = \exp \left[-\frac{\omega}{2U} \int \delta Q^{-1} ds \right], \quad (3)$$

where the integration is performed along the great-circle ray path connecting the i th source and the j th station, $\delta Q^{-1}(\omega)$ is the perturbation in attenuation at angular frequency ω , and $U(\omega)$ is the reference group velocity. It is understood that eq. (3) applies at a specific frequency ω which is dropped hereinafter in similar cases. Following DE06, the lateral variations in attenuation are expanded in spherical harmonics to degree L_Q , and eq. (3) is implemented as

$$A_{ij}^Q = \exp \left[-\frac{\omega X_{ij}}{2U} \sum_{l=0}^{L_Q} \sum_{m=-l}^l q_{lm} \overline{Y_{lm}^{ij}} \right], \quad (4)$$

where X_{ij} is the path length in km, q_{lm} are the coefficients to be determined, and $\overline{Y_{lm}^{ij}}$ is the path-averaged spherical-harmonic function.

We predict the effect of focusing on amplitude (A_{ij}^F) by applying three different theoretical approaches to the Rayleigh wave phase-velocity maps. For GCRA, the relationship between amplitude and the relative perturbation in phase velocity is given by

$$\ln A_{ij}^F = \frac{\delta c_i}{2c_0} + \frac{\delta c_j}{2c_0} + \frac{1}{2 \sin \Delta} \int_0^\Delta [\sin(\Delta - \phi) \sin \phi \partial_\theta^2 - \cos(\Delta - 2\phi)] \frac{\delta c}{c_0} d\phi, \quad (5)$$

where Δ , θ , and ϕ are the epicentral distance, along-path coordinate, and path-perpendicular coordinate, respectively, and $\frac{\delta c_i}{2c_0}$ and $\frac{\delta c_j}{2c_0}$ are the perturbation in phase velocity at the source and receiver, respectively (Woodhouse & Wong 1986; Dahlen & Tromp 1998; DE06). The ERT amplitude is determined by solving the dynamic ray-tracing equations (e.g. Larson *et al.* 1998). For 2-D FFT, the amplitude due to focusing is estimated by integrating the phase-velocity perturbation over the unit sphere Ω :

$$\ln A_{ij}^F = \int \int_\Omega K_A^C(\theta, \phi) \frac{\delta c}{c_0}(\theta, \phi) d\Omega. \quad (6)$$

The quantity K_A^C is the 2-D single-frequency kernel that expresses the sensitivity of Rayleigh wave amplitude to phase velocity (Zhou *et al.* 2004). It is described as

$$K_A^C = -\frac{2k^{3/2} \cos[(\Delta' + \Delta'' - \Delta) + \pi/4]}{\sqrt{8\pi} |\sin \Delta'| |\sin \Delta''| / |\sin \Delta|}, \quad (7)$$

where k is the wavenumber on the unit sphere, and Δ' , Δ'' and Δ denote the source-to-scatterer, scatterer-to-receiver, and source-to-receiver great-circle angular path lengths, respectively (Zhou *et al.* 2004). Source-radiation and receiver-polarization factors are as-

sumed to be the same along the source-to-scatterer and scatterer-to-receiver legs of the propagation path.

Given a set of focusing-amplitude predictions, the spherical-harmonic maps of attenuation can thus be simultaneously determined along with the source and receiver correction terms using following expression:

$$\begin{aligned} & -\frac{2U}{\omega X_{ij}} (\ln A_i^S + \ln A_j^R) + \sum_{l=0}^{L_Q} \sum_{m=-l}^l q_{lm} \overline{Y_{lm}^{ij}} \\ & = -\frac{2U}{\omega X_{ij}} \ln \frac{A_{ij}}{A_{ij}^F}. \end{aligned} \quad (8)$$

We follow DE06 and constrain the sum of $\ln A_j^R$ values to zero in order to reduce the trade-off between the mean values of the source and receiver factors.

4 FOCUSING PREDICTIONS

The phase-velocity maps derived from the selected path-averaged phase-velocity measurements (Table S1) are shown in Fig. 2. Variance reduction of the phase observations is calculated from the difference between the observed and predicted path-averaged phase velocity (e.g. eq. 18 of DE06). The variance reduction provided by the 50-s maps is 90 and 89 per cent for degree-40 and degree-20, respectively; these values are 84 and 83 per cent at 100 s. Those maps are compared with the GDM52 model (Ekström 2011) in Fig. 2. At both periods the power spectra are highly similar, and cumulative correlation coefficients up to degree 40 between our model and GDM52 are >0.94 .

We then predict the focusing effects from the phase-velocity maps and the three approximate theories: GCRA, ERT and FFT. The values of $\ln A_{ij}^F$ that result from these predictions are compared in Figs 3 and 4 for 50 s and Figs S1 and S2 for 100 s, based on the corresponding degree-20 and degree-40 phase-velocity maps, respectively. The focusing predictions from the degree-20 and degree-40 phase-velocity maps of 50 and 100 s are compared in Figs 5 and S3, respectively. We present the comparisons with two visualizations: a scatter plot with an individual symbol for each path, and a 2-D histogram to illustrate the density of points in the scatter plot. These comparisons highlight four important points. (1) For all comparisons, the 2-D histograms reveal that the agreement is generally better than is apparent in the scatter plots. The nearly 400 000 individual symbols on the scatter plot tend to accentuate outliers and obscure information about the density of points. (2) The relationship between the GCRA and FFT predictions is nearly linear. At 50 s the correlation coefficient between GCRA and FFT predictions is 0.92 for the degree-20 maps and 0.84 for the degree-40 maps. Both approaches contain the assumption of propagation along the great circle, and in both cases the focusing prediction varies linearly with the phase-velocity perturbation; these two factors help explain the observed relationship. At 50 s, FFT-predicted amplitude anomalies tend to be larger than GCRA- and ERT-predicted amplitudes, especially for the degree-20 phase-velocity map. At 100 s the amplitude anomalies show similar magnitudes for the degree-20 maps and stronger magnitudes for GCRA and ERT relative to FFT for the degree-40 maps. (3) The relationships between GCRA and ERT predictions, and between FFT and ERT predictions, are nonlinear, and there are strong disagreements for some paths. Larson *et al.* (1998) has shown that the ERT predictions are log-normally distributed whereas the GCRA predictions are normally distributed. The different distributions give rise to the nonlinear relationship. A similar explanation applies to the FFT versus ERT comparison.

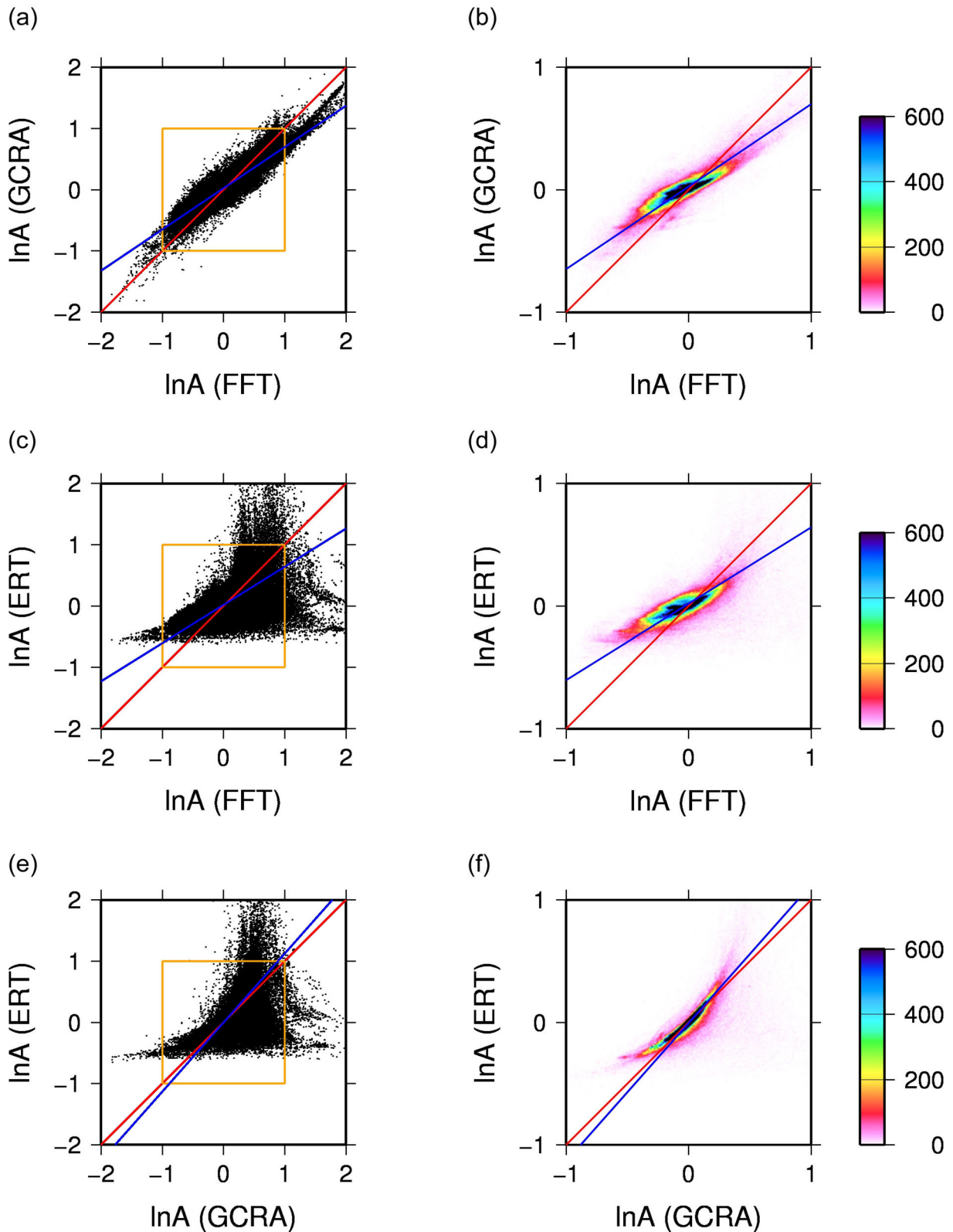


Figure 3. Comparison of focusing effects ($\ln A^F$) predicted using three approximate theories (GCRA, ERT and FFT) for the degree-20 phase velocity map of 50 s period. (a, c, e) show comparison as a scatter plot; blue line shows best-fitting line determined using orthogonal regression. (b, d, f) show 2-D histogram of area within yellow boxes to highlight the density of points, which is not apparent in the scatter plots.

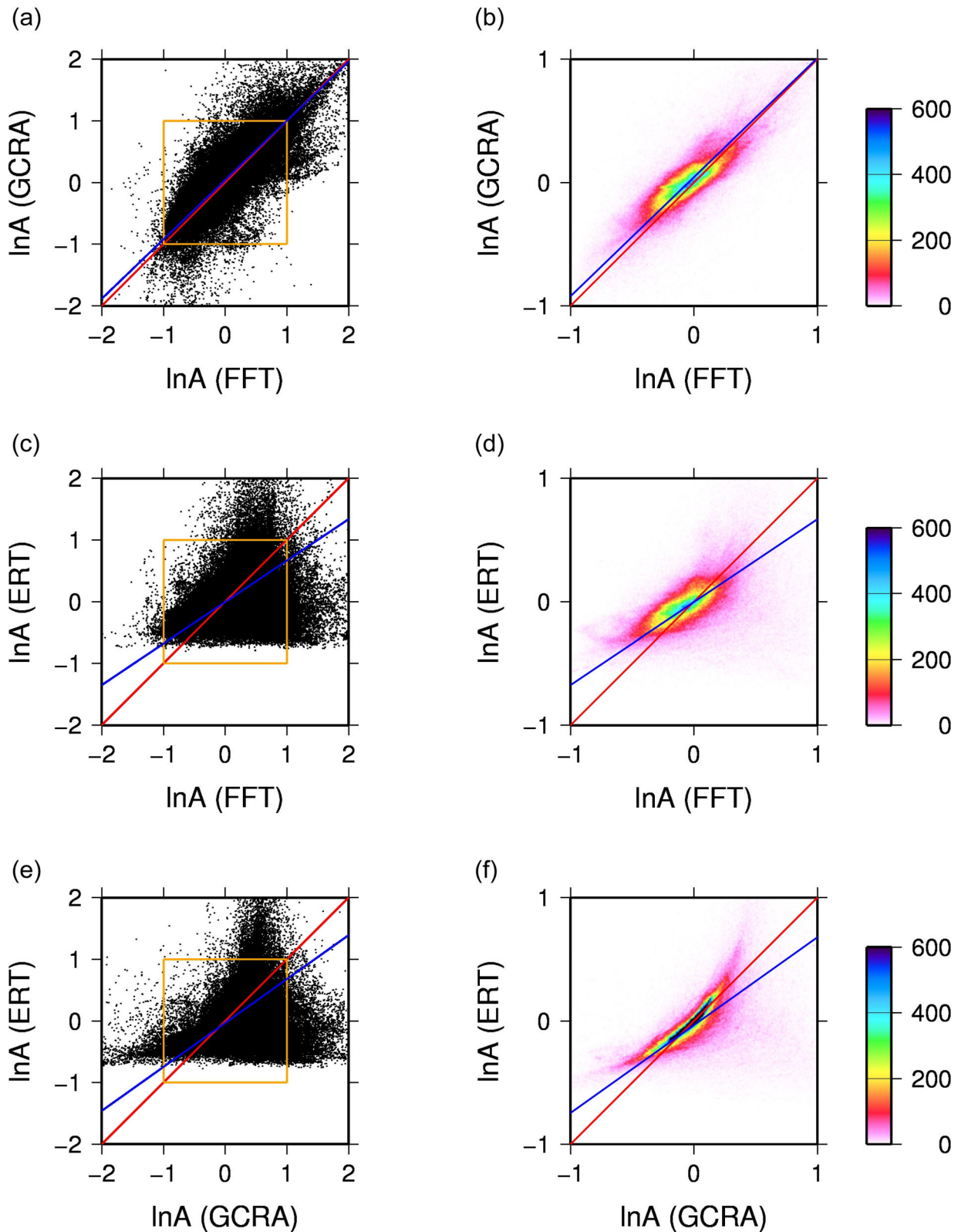


Figure 4. Same as in Fig. 3 but for degree-40 phase velocity map of 50 s period.

However, the 2-D histograms show that for many paths the two sets of predictions are nearly linear, a conclusion that is not obvious from the scatter plot. (4) The predictions made using degree-40 maps show stronger disagreement between the approximate theories than those made using degree-20 maps, especially at 50 s, as a re-

sult of the rougher heterogeneity contained in the higher-resolution maps.

Focusing predictions made using the degree-20 and degree-40 phase-velocity maps show the best agreement for FFT (Figs 5 and S3); the ERT and GCRA predictions are more strongly dependent

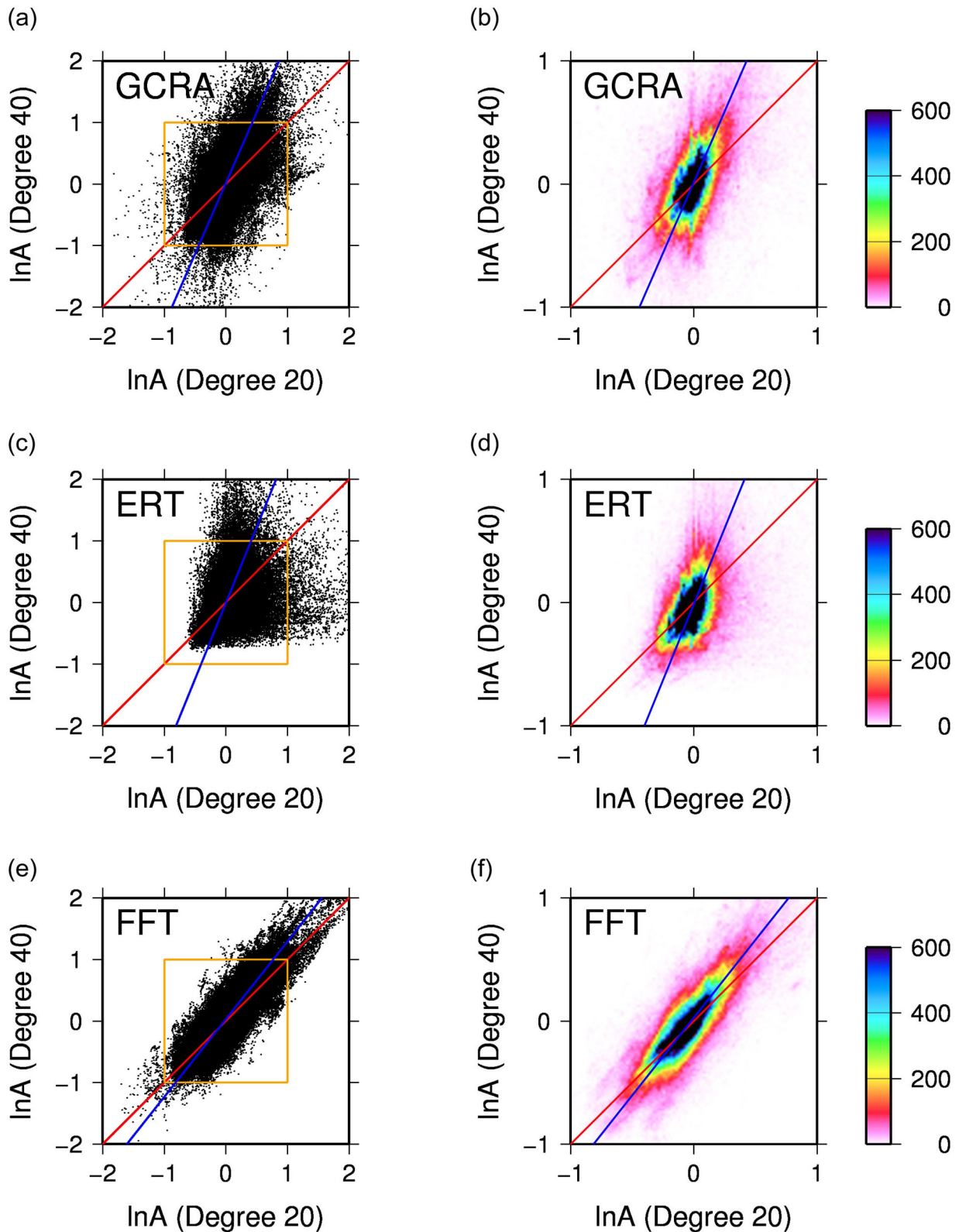


Figure 5. Comparison of predicted focusing effects for the same approximate theory but with different spherical-harmonic expansions (degree-20 and degree-40) in the phase-velocity maps of 50 s period. (a), (c) and (e) show scatter-plot comparison for GCRA, ERT and FFT, respectively. (b), (d) and (f) show 2-D histogram of area within yellow boxes for GCRA, ERT and FFT, respectively.

on the maximum degree of the spherical-harmonic expansion. Ma *et al.* (2016) reached a similar conclusion from their comparison of predicted amplitudes. Because the FFT prediction is calculated by integrating the sensitivity within the Fresnel zone, the roughness of the phase-velocity anomalies has a smaller effect than it does for the GCRA and ERT predictions, which depend on the second derivative of phase velocity (e.g. eq. 5). The best-fitting lines, calculated from the degree-20 and degree-40 comparisons and determined using orthogonal regression, have slopes of 2.30, 2.46 and 1.26 for GCRA, ERT and FFT, respectively, at 50 s (Fig. 5) and 1.57, 1.64 and 1.16 at 100 s (Fig. S3). These values help to quantify the strong dependence of the GCRA and ERT focusing predictions on the roughness of the phase-velocity map, especially at 50 s.

5 ATTENUATION MAPS

Rayleigh wave attenuation maps are obtained by applying eq. (8) to the amplitude data. The predicted focusing effects are removed from each datum prior to the inversion; this is the approach taken in one of our earlier studies (Dalton *et al.* 2008). Previous studies have accounted for focusing effects during the inversion (rather than prior to the inversion) by allowing the amplitudes to help constrain the phase-velocity maps (DE06; Ma *et al.* 2016). In Fig. S4, we show that the effect of this choice on the attenuation structure is negligible; the correlation coefficient between 50-s attenuation maps determined by accounting for focusing effects during versus prior to the inversion is 0.96 at degree 12. Figs 6 and S5 show the attenuation maps for 50 and 100 s, respectively. Six sets of maps are obtained at each period, corresponding to the three approximate theories (GCRA, ERT, FFT) and the two spherical-harmonic expansions of the phase-velocity maps (degree-20 and degree-40) used for the focusing predictions. We follow DE06 and Dalton *et al.* (2008) and expand the attenuation maps in spherical harmonics to degree 12. We also apply a roughness-minimization constraint to the attenuation maps. In Section 6, we discuss the sensitivity of the data misfit to these assumptions. The same level of damping (i.e. same value of the damping coefficient) was applied to all attenuation maps in Figs 6 and S5. Figs S6 and S7 explore differences between the six sets of maps in more detail. Since both the current study and our earlier work (Dalton *et al.* 2014) have shown that focusing is most accurately predicted using ERT and degree-20 maps at 50 s and FFT and degree-40 maps at 100 s, we express the differences relative to those maps. The source and receiver terms are also determined from this inversion, as shown in Fig. S8. The magnitude and geographical distribution of these terms vary little when focusing effects are predicted with other approximate theories and map expansions.

The six 50-s attenuation maps (Fig. 6) contain many features in common. The highest attenuation is found along the East Pacific Rise and western North America; many other parts of the global ridge system and several of the subduction zones in the western Pacific are also characterized by above-average attenuation. Stable continental interiors, including eastern North America, western Australia, and northern Eurasia, exhibit below-average attenuation in all six maps. The correlation coefficient between each pair of maps and the power in each map are summarized in Table S2 and Fig. S9(a), which demonstrate that the large-scale attenuation features are robustly imaged in all maps and that the maps for which focusing predictions are calculated using FFT contain stronger heterogeneity than when focusing predictions are calculated using GCRA and ERT. Stronger heterogeneity in the maps with FFT focusing

predictions is consistent with the comparison of focusing-predicted amplitudes in Figs 3 and 4: for both the degree-20 and degree-40 phase-velocity maps, the FFT-predicted amplitudes span a greater range of values than the GCRA- and ERT-predicted amplitudes. Since the focusing-predicted amplitudes are removed from the observed amplitudes prior to inversion (eq. 8), the attenuation maps derived from amplitudes from which FFT-predicted values have been removed contain larger variations. The six 100-s attenuation maps (Fig. S5) are also highly similar to one another; their correlation coefficients and power spectra are summarized in Table S3 and Fig. S9(b). The strength of heterogeneity is more consistent between the maps than is the case at 50 s.

Figs 3 and 4 show larger focusing-predicted amplitudes for FFT than for GCRA and ERT at 50 s period. This difference manifests in stronger attenuation anomalies in Figs 6(e) and (f) for which focusing effects are predicted with FFT. Fig. 5 shows larger focusing-predicted amplitudes for degree-40 maps than degree-20 maps when GCRA and ERT are used; however, in this case the attenuation anomalies have a similar magnitude in the maps for which focusing effects are predicted with GCRA and the degree-20 map versus GCRA and the degree-40 map (Fig. 6). Thus, while the regression line helps to describe the nature of the relationship between two sets of focusing-predicted amplitudes, it alone cannot be used to understand how the features in the attenuation maps will be affected. The differences in the degree-20 and degree-40 focusing predictions are entirely due to small-scale anomalies in the degree-40 phase-velocity maps, since the long-wavelength features in the maps are identical. The focusing-predicted amplitude differences will therefore depend on the specifics of the propagation path, for example what anomalies it traverses and from what direction, yielding differences that are mostly uncorrelated from path to path and the greater scatter apparent in Figs 5 and S3. It seems that the relatively low spherical-harmonic expansion of the attenuation maps (degree 12) smooths out much of this signal and causes little net effect on the attenuation maps. On the other hand, the differences in the GCRA and FFT focusing predictions result from differences in the underlying theory. They might therefore be expected to be correlated from path to path, consistent with the lesser scatter apparent in Figs 3 and 4 and Figs S1 and S2, and to have an overall effect on the attenuation maps, as observed.

6 DISCUSSION

6.1 Importance of source, receiver and focusing terms

Fig. 7 shows distributions of the A^Q , A^F , A^S and A^R values for period of 50 s and with focusing effects predicted using ERT and the degree-40 phase-velocity map. This comparison demonstrates that the focusing and source contributions to an observed amplitude are typically the largest, followed by attenuation; for most paths the receiver term is relatively small.

Figs 8 and S10 explore the influence that the source and receiver terms and corrections for focusing effects have on the retrieved attenuation maps. Fig. 6(a) (50 s, degree-20 phase velocity map, focusing effects predicted from GCRA) and S5a (100 s, degree-20 phase velocity map, focusing effects predicted from GCRA) are used as references, which are plotted again as Figs 8(a) and S10(a) for convenience. The same damping coefficient was applied to all maps in these figures. Figs 8(c) and S10(c) show the attenuation maps obtained when it is assumed that Rayleigh wave amplitudes are due only to variations in attenuation; the source, receiver, and

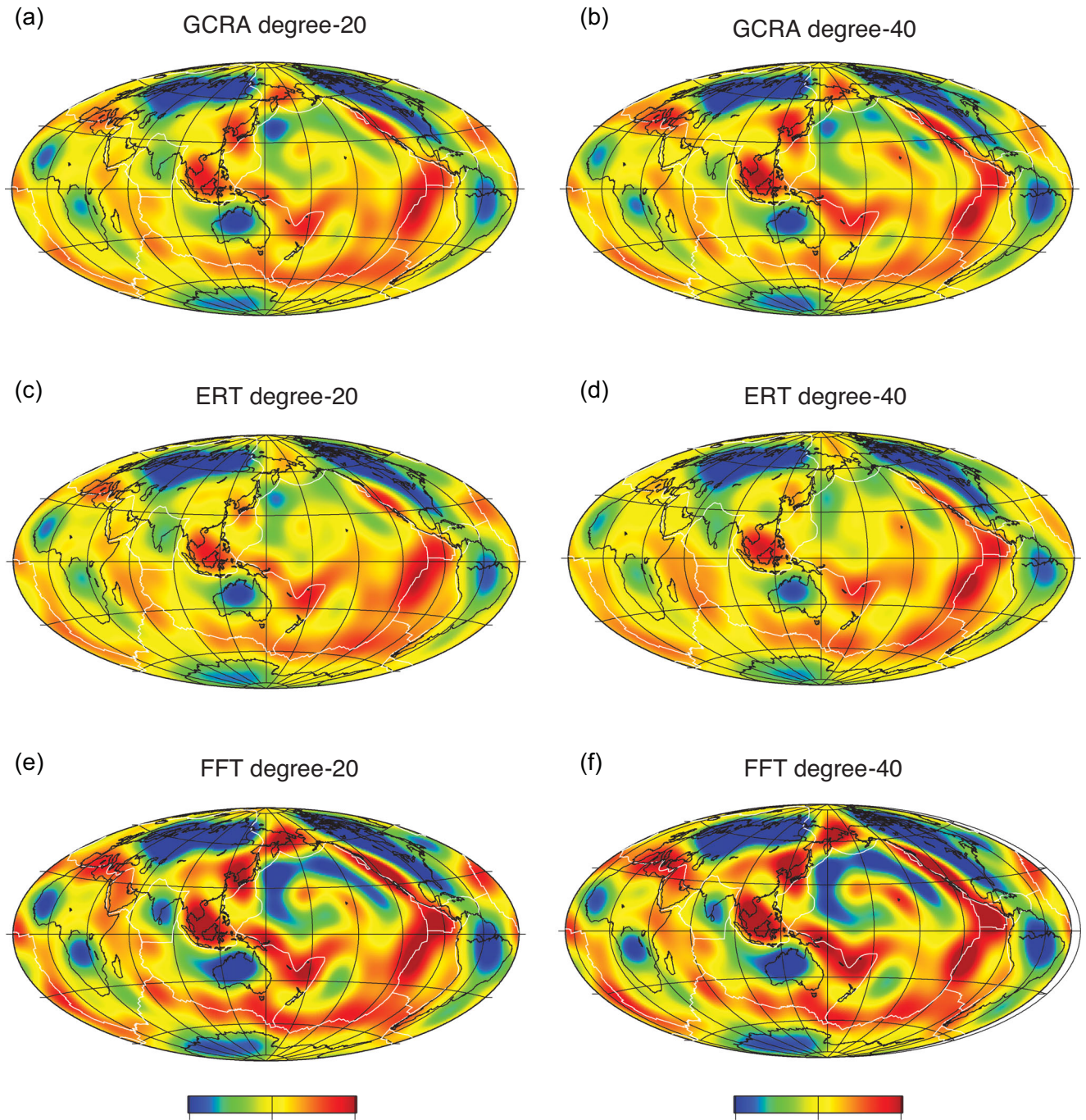


Figure 6. Attenuation maps for 50-s Rayleigh waves. The six maps were obtained under identical conditions except for the approximate theory and expansion of the phase-velocity map used for the prediction of focusing effects. (a) GCRA and degree-20 phase-velocity map. (b) GCRA and degree-40 phase-velocity map. (c) ERT and degree-20 phase-velocity map. (d) ERT and degree-40 phase-velocity map. (e) FFT and degree-20 phase-velocity map. (f) FFT and degree-40 phase-velocity map. Source and receiver terms were also solved for in the inversion.

focusing terms in eq. (8) are all ignored. Figs 8(b) and S10(b) show the maps obtained the observed amplitudes are attributed to variations in attenuation and focusing effects while source and receiver terms are ignored; the main patterns in these maps are significantly similar those in Figs 8(a) and S10(a).

Comparison of Figs 8(b) and (c) highlights the specific features that are altered by accounting for focusing effects. The largest changes are in the northern hemisphere between longitudes of 90°E and 270°E . When focusing effects are accounted for, attenuation along the Pacific continental margin is significantly enhanced;

the channel of low phase velocities that characterizes this region (Figs 2a–c) likely causes focusing of Rayleigh wave amplitudes that is mapped into anomalously low attenuation when focusing effects are ignored. The defocusing that occurs on either side of this low-velocity channel reduces Rayleigh wave amplitudes and is mapped into anomalously high attenuation when focusing effects are ignored. Accounting for focusing effects due to propagation through low-velocity channels also enhances attenuation in several places along the mid-ocean-ridge system, for example in the southernmost Pacific–Antarctic Ridge, the easternmost Southeast Indian Ridge,

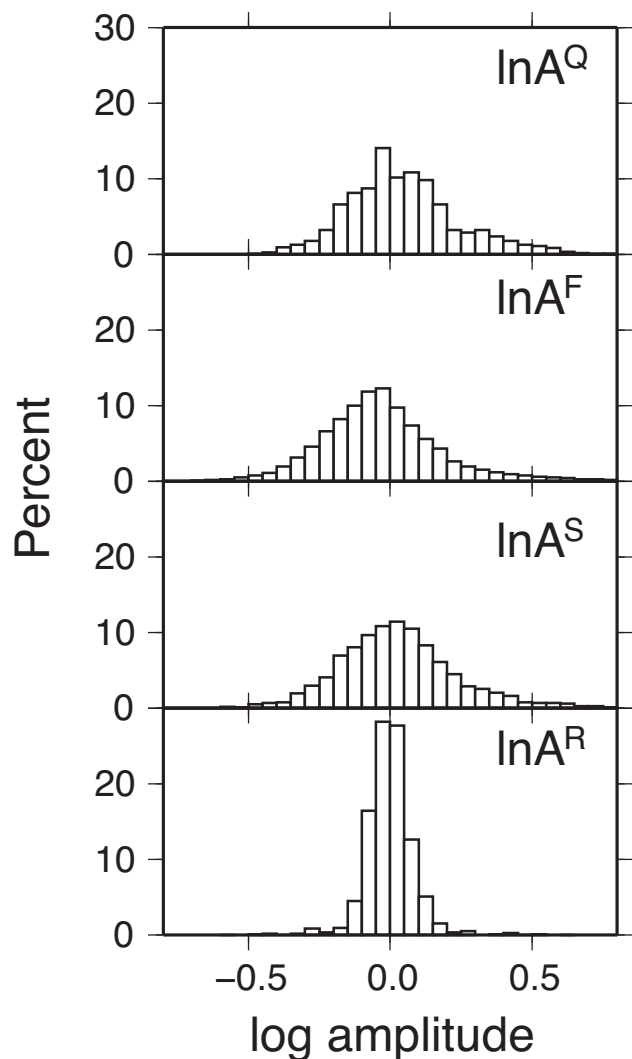


Figure 7. Histograms showing the distribution of $\ln A^Q$, $\ln A^F$, $\ln A^S$ and $\ln A^R$ from the inversion of degree-12 attenuation map of 50 s period for focusing predicted with ERT and degree-40 phase velocity map.

and the Mid-Atlantic Ridge. Accounting for defocusing effects due to propagation through high-velocity regions reduces attenuation in almost all areas of Archean and Proterozoic crust.

In Figs 8(d) and S10(d) we show attenuation maps obtained when source and receiver terms are included in the inversion but the focusing correction is excluded. Comparison of Figs 8(d) and (c) highlights the specific features that are altered by accounting for source and receiver effects. The differences are generally slight, indicating that source and receiver terms have a smaller effect on the attenuation structure in Figs 6 and S5 than the focusing effects do. Source or receiver terms that are larger than unity indicate that the actual source or receiver amplitude is larger than the source or receiver amplitude predicted by PREM. If source and receiver effects on amplitude are ignored, the large amplitude values map into anomalously low attenuation, and the opposite is true for source and receiver terms that are smaller than one. Accounting for source and receiver effects slightly reduces attenuation in the vicinity of Hawaii; this is an area where source and receiver terms are generally <1 (Fig. S8), indicating that PREM overestimates source and receiver amplitudes, which will map into anomalously high attenuation if source and receiver effects are ignored. On the other hand,

accounting for source and receiver effects slightly enhances attenuation just north of the India–Eurasia Plate boundary. In this area the source and receiver terms are generally >1 (Fig. S8); PREM underestimates the source and receiver amplitudes, which will map into anomalously low attenuation if source and receiver effects are ignored.

Whereas Fig. 8 assesses the effects of focusing and source and receiver terms relative to the case where all are ignored, Fig. 9 assesses their influence relative to the case where all are considered. Fig. 9(a) shows features that are changed by the exclusion of focusing, source, and receiver effects, and Fig. 9(c) shows features that are changed when only focusing is ignored. Figs 9(b) and (d) demonstrates that neglecting focusing effects has a more profound impact on the maps at higher spherical-harmonic degrees; the low-degree (long-wavelength) attenuation features can be faithfully retrieved. Dalton *et al.* (2014) reached a similar conclusion from their inversion of synthetic Rayleigh wave amplitudes: the long-wavelength features (degree <6) of the input attenuation maps were nearly perfectly recovered but the shorter-wavelength features were corrupted by focusing effects. For the 100-s comparison (Fig. S11), the two maps are well correlated at degrees <6 but de-correlated at higher degrees. The difference maps highlight higher attenuation along the mid-ocean ridges, western North America, and the western Pacific and lower attenuation in the Pacific basin and stable cratonic areas in the maps in Figs 6(a) and S5(a) relative to Figs 8(c) and S10(c).

To understand how focusing effects can masquerade as attenuation structure if not correctly treated, we invert the focusing-predicted amplitudes for degree-12 attenuation maps (Figs 10 and S12). The six sets of 50-s maps contain similar features, although stronger anomalies are obtained from inverting the FFT-predicted amplitudes than the GCRA- and ERT-predicted amplitudes. This is consistent with our observation that the 50-s attenuation maps for which focusing effects were predicted with FFT contain stronger heterogeneity (Fig. 6). Many of the features in Figs 10 and S12 can be related to large horizontal gradients in phase velocity. For example, the pronounced low-velocity zone along western North America results in focusing of Rayleigh waves and high amplitudes. High amplitudes, if interpreted in terms of attenuation instead of focusing, map into low-attenuation features, as can be seen along western North America.

If the attenuation maps obtained when source and receiver terms are included in the inversion but the focusing correction is excluded (Figs 8d and S10d) contain a large signal due to focusing effects and if the amplitudes due to focusing effects predicted with GCRA, ERT or FFT are sufficiently accurate, we would expect a correlation between the maps in Figs 10 and 8(d), and Figs S12 and S10(d), respectively. Figs 11 and S13 show the correlation coefficient at each degree for 50 and 100 s, respectively. At degrees <7 the maps are generally de-correlated or somewhat anti-correlated. However, at higher degrees the correlation becomes steadily more positive, indicating contamination of the attenuation maps in Figs 8(c), (d) and S10(c), (d) by unmodelled focusing effects.

6.2 Error estimation

We calculate the variance reduction vr_{amp} to assess the ability of the inversion results to fit the amplitude observations:

$$vr_{\text{amp}} = 1 - \frac{\sum_{k=1}^N (q_k^{\text{obs}} - q_k^{\text{pred}})^2}{\sum_{k=1}^N (q_k^{\text{obs}})^2}, \quad (9)$$

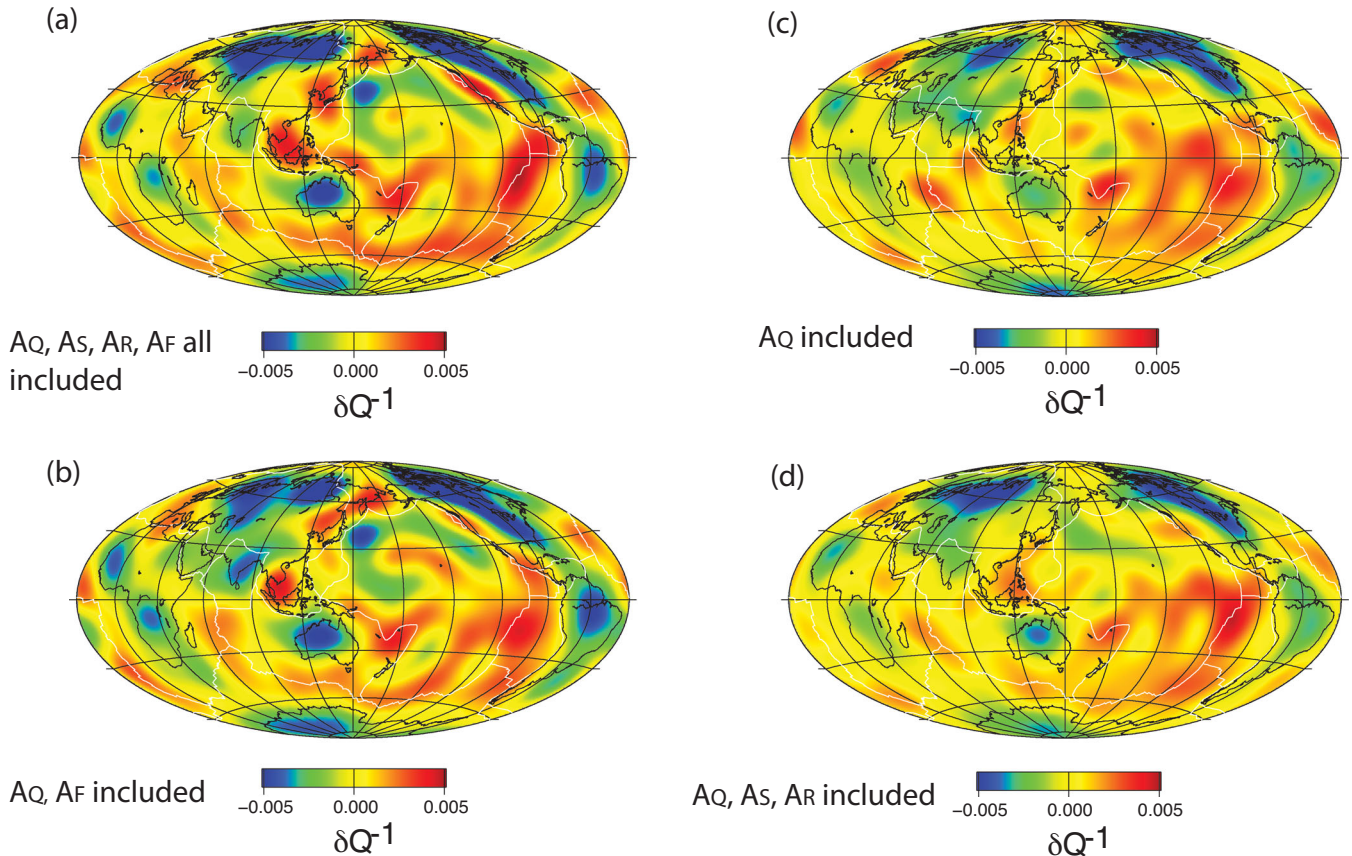


Figure 8. Comparison of 50-s attenuation maps obtained with and without corrections for source, receiver, and focusing effects. (a) As in Fig. 6(a), the amplitude observations are attributed to attenuation, source, receiver, and focusing effects (GCRA, degree 20). (b) Both attenuation and focusing effects are considered; source and receiver effects are ignored. (c) Only attenuation is considered in the inversion; source, receiver and focusing effects are all ignored. (d) Attenuation, source, and receiver effects are considered; focusing effects are ignored.

where

$$q_k^{\text{obs}} = -\frac{2U}{\omega X_k} \ln A_k, \quad (10)$$

and

$$q_k^{\text{pred}} = -\frac{2U}{\omega X_k} (\ln A_k^S + \ln A_k^R + \ln A_k^F) + \sum_{l=0}^{L-Q} \sum_{m=-l}^l \delta Q_{lm}^{-1} \overline{Y_{lm}^k}. \quad (11)$$

Here N is the total number of amplitude measurements.

The variance reduction for the 50-s and 100-s amplitude data sets primarily depends on three factors: (1) the strength of damping applied to the attenuation coefficients; (2) the maximum degree of the spherical-harmonic expansion of the attenuation map; (3) the approximate theory and phase-velocity map used for the prediction of focusing effects. Of these three factors, the strength of damping has the smallest effect; in fact, we obtain a reasonable attenuation map without any damping at all. The plot of variance reduction as a function of damping parameter takes the shape of an L-curve: higher (lower) variance reduction for small (large) damping parameters and a steeper (shallower) fall-off at small (large) damping parameters, with a corner at the transition from steep to shallow. Like many studies of this nature, we select the optimal damping factor (0.005) at the position of the corner. To illustrate the relatively minor influence of this decision we note that variance reduction decreases by only 1 per cent when the damping factor is increased from 0 to 0.01

for the degree-12 50-s attenuation map determined with focusing predictions using GCRA and the degree-20 phase-velocity map.

The influence of the other two factors on variance reduction is shown in Fig. 12; the optimal damping factor (0.005) is used for these calculations. Maximum degree of the spherical-harmonic expansion for the attenuation maps is varied (4, 8, 12, 16, 20), and the six sets of focusing predictions (degree-20 and degree-40 phase-velocity maps with GCRA, ERT, and FFT approximate theories) are considered. As expected, the variance reduction improves with maximum degree of the spherical-harmonic expansion of the attenuation maps; the number of unknown coefficients increases from 25 to 441 as the degree increases from 4 to 20. We use an F-test to confirm that each incremental variance-reduction improvement (e.g. as degree increases from 4 to 8, or from 8 to 12, etc.) is statistically significant at the 95 per cent confidence level, meaning that the change in variance reduction results from more than just a larger number of unknown parameters. Instead, the inclusion of smaller-scale heterogeneity in the attenuation maps provides a better fit to the amplitude observations.

At a fixed degree of the expansion of the attenuation maps, differences in variance reduction are due to differences in the predicted focusing amplitudes, and presumably higher variance reduction can be attributed to predicted focusing amplitudes that more faithfully represent actual focusing effects in the real Earth. For example, FFT-predicted amplitudes using degree-20 and degree-40 phase-velocity maps are highly similar (Figs 5 and S3); not surprisingly, the corresponding variance-reduction values are also quite similar

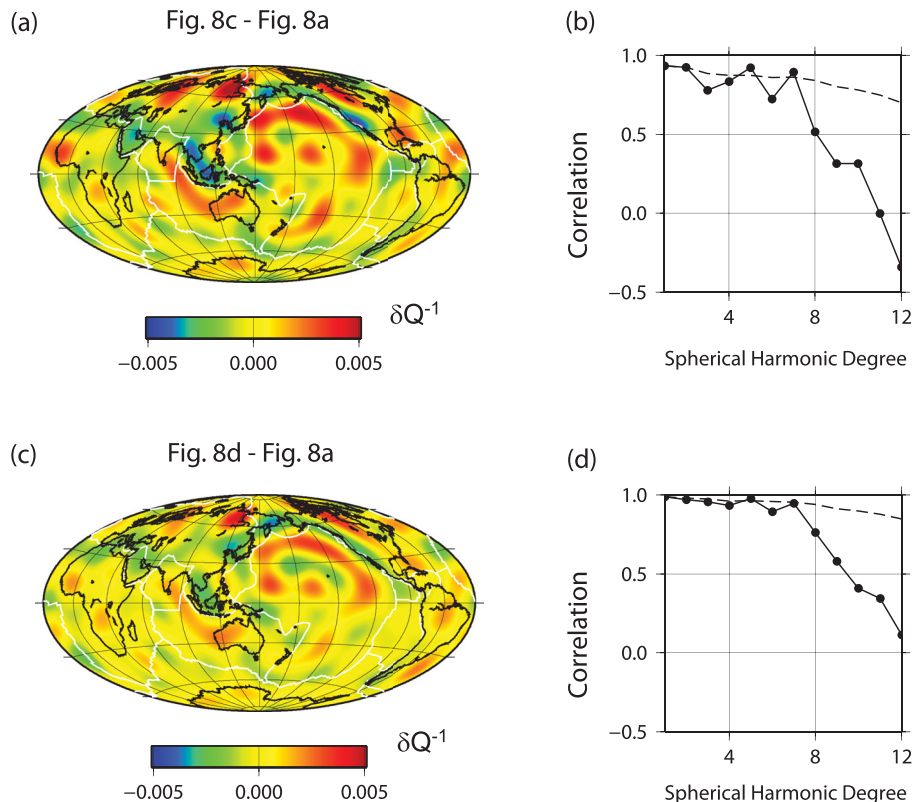


Figure 9. The effect on attenuation structure of including or ignoring focusing effects. (a) This difference map highlights the effect of accounting for focusing, source, and receiver effects. Positive (negative) values indicate that attenuation is lower (higher) when these effects are accounted for. (b) Correlation coefficient at each spherical-harmonic degree (solid line with black dots) and cumulative correlation coefficient (dashed line) between maps in Figs 8(c) and (a). (c) This difference map highlights the effect of accounting for focusing effects. (d) Correlation coefficient at each spherical-harmonic degree (solid line with black dots) and cumulative correlation coefficient (dashed line) between maps in Figs 8(d) and (a).

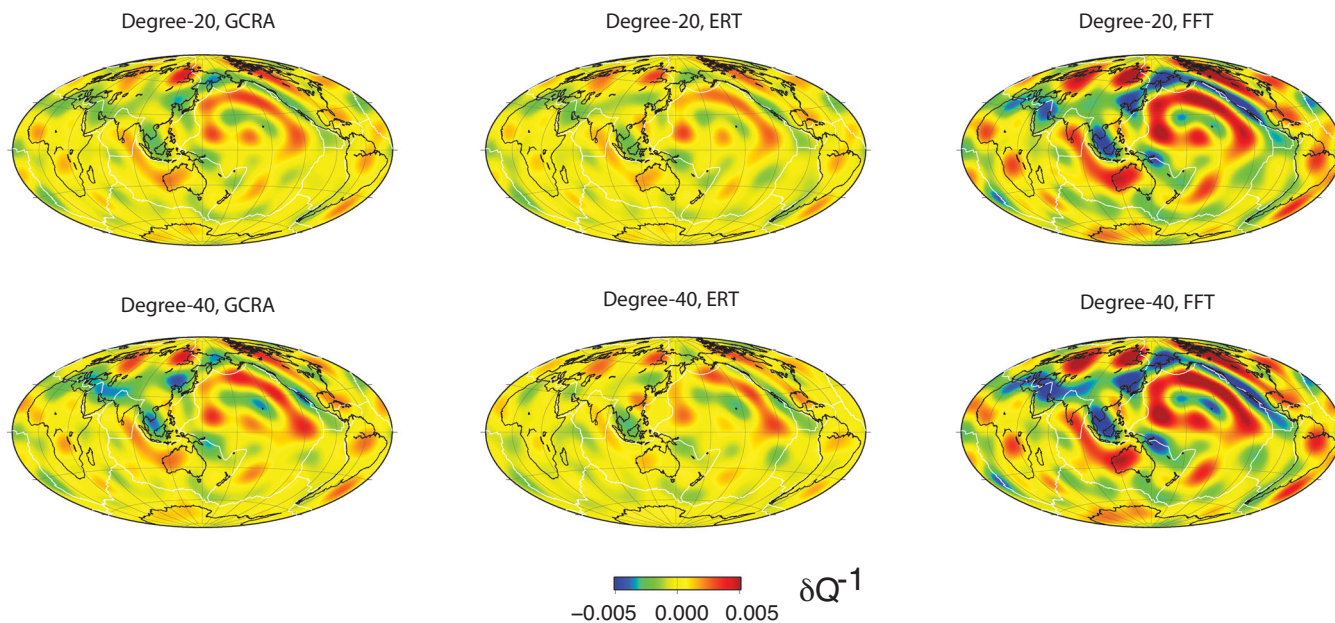


Figure 10. Demonstration of how focusing effects will be mapped into anomalous attenuation structure if not accounted for. Maps are obtained by inverting the focusing-predicted amplitudes in Figs 3 and 4 for degree-12 attenuation maps at 50 s. Note that no amplitude measurements are used to derive these maps.

(Fig. 12). At 50 s, the GCRA- and ERT-predicted amplitudes using degree-20 phase-velocity maps yield nearly identical variance reductions, as expected given the similarity of the two sets of focusing predictions (Fig. 3f). At 50 s, the two ray-based theoretical approx-

imations, GCRA and ERT, yield focusing predictions that provide the best variance reduction to the amplitude observations; for attenuation maps expanded to degree 16 and larger, variance reduction with FFT-based focusing predictions overlaps with these two.

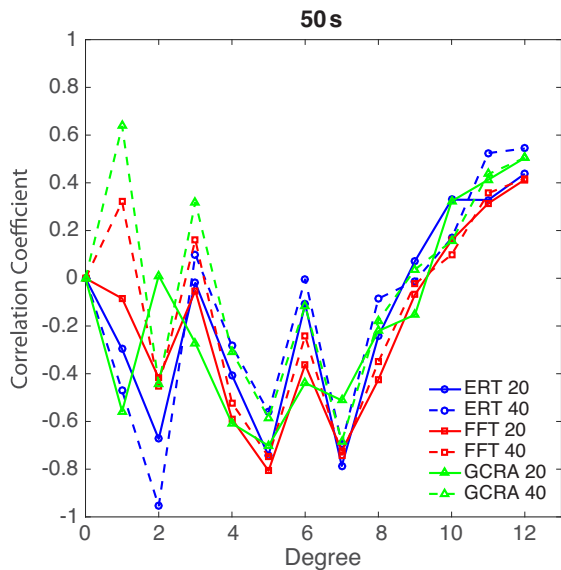


Figure 11. Correlation coefficient at each spherical-harmonic degree between Figs 8(d) and 10.

Focusing predictions using degree-40 phase-velocity maps rather than degree-20 maps result in weaker variance reduction for all scenarios. At 100 s, FFT-based focusing predictions provide the strongest variance reduction for all scenarios, with slightly higher values for the degree-40 phase-velocity maps.

These results agree with well the conclusions reached by Dalton *et al.* (2014) in their study of Rayleigh wave amplitudes mea-

sured from synthetic waveforms that were generated using a 3-D elastic model and 1-D anelastic model. In that earlier study, the effects of source excitation and receiver amplification were removed from the amplitude measurements so that the remaining signal could be attributed to elastic propagation effects; these corrected measurements were compared to predicted focusing amplitudes. Dalton *et al.* (2014) found that at shorter periods (50 s) ERT most accurately predicted focusing effects whereas at longer periods (125 s) FFT was most successful. While GCRA was least successful at all periods, it performed especially poorly when the 3-D elastic model contained strong short-wavelength heterogeneity. In the present study we find that the ray-based approaches generally perform better than the finite-frequency kernels at 50 s and that using GCRA with a degree-40 phase-velocity map explains very little of the variance in the amplitude observations. At longer periods FFT performs better than either ray-based approach. Both sets of results indicate that the approximation of the surface wave as a thin ray that can bend according to local velocity structure is more appropriate than a broad kernel that is symmetric about the great-circle path for the short-wavelength high-frequency surface waves. For long-wavelength low-frequency surface waves, the opposite is true: the broad sensitivity zone is more important for representing focusing effects than the ray-bending effects. In contrast to the earlier study, we see less difference between GCRA and ERT, especially when the degree-20 phase-velocity maps are used. One explanation for this discrepancy may be the extent to which the phase-velocity maps faithfully represent actual Earth structure. In the earlier study of synthetic waveforms the 3-D elastic model is prescribed and therefore perfectly known; in the current study the phase-velocity maps are determined from travel-time measurements

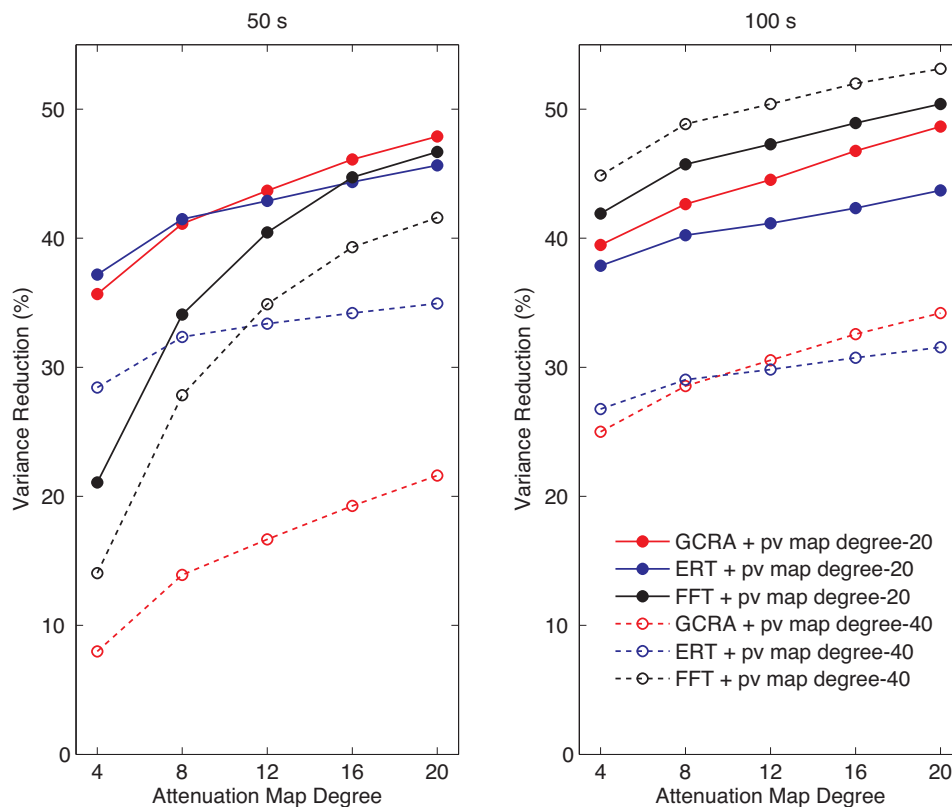


Figure 12. Variance reduction of the amplitude observation for different inversion results at (left-hand panel) 50 s and (right-hand panel) 100 s. The spherical-harmonic expansion of the attenuation maps and the approximate theory and phase-velocity map expansion utilized for the prediction of focusing amplitudes are varied. Red, blue, and black lines and symbols represent GCRA, ERT and FFT, respectively.

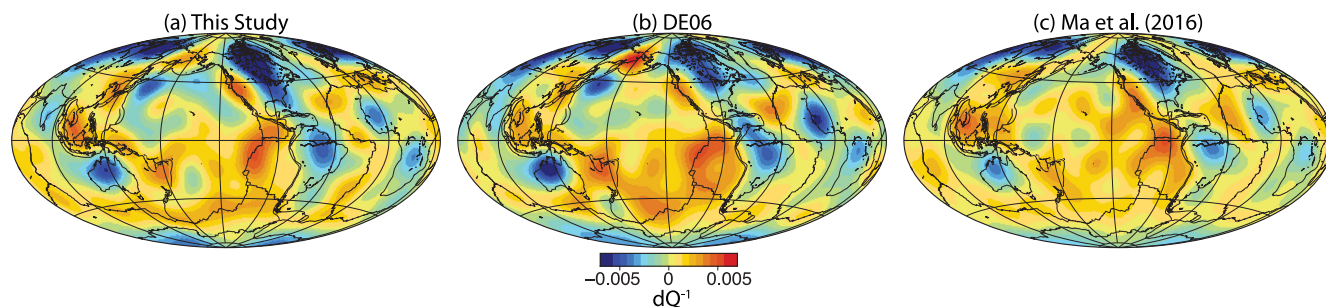


Figure 13. Comparison of 50-s Rayleigh wave attenuation maps, here expanded to spherical-harmonic degree 12. (a) From this study, with focusing effects predicted using GCRA and the degree-20 phase velocity map. (b) From DE06. (c) From Ma *et al.* (2016). Note that similar attenuation patterns are shown in all models, but our model resolves the relatively weak attenuation to the east of the New Zealand.

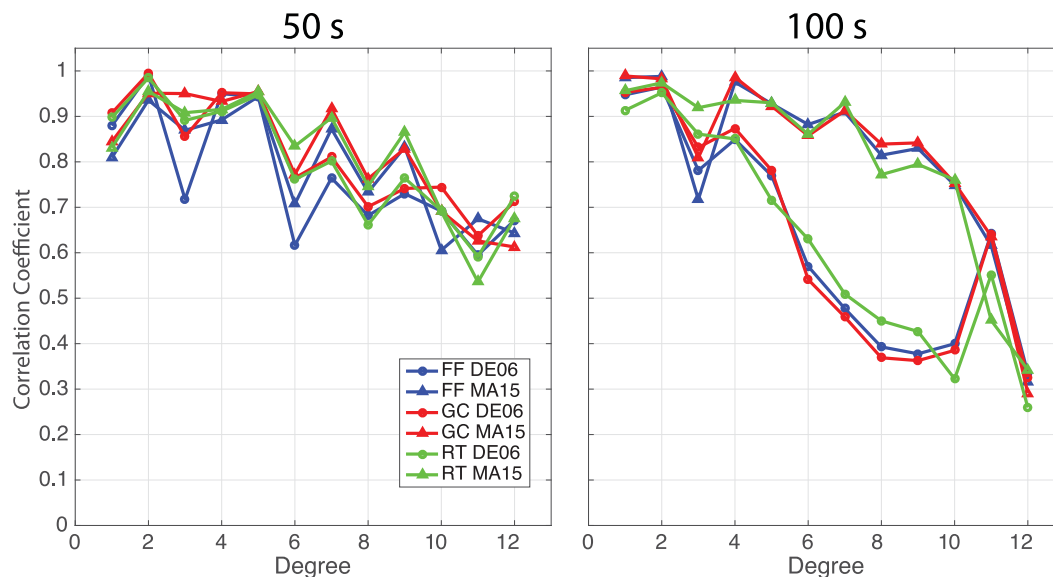


Figure 14. Correlation coefficient at each spherical-harmonic degree between the maps of this study (Figs 6 and S5) and earlier results of DE06 and Ma *et al.* (2016). In this comparison the maps of this study have had focusing effects predicted with degree-20 phase-velocity maps.

and contain the assumption of propagation along the great-circle path.

6.3 Comparison with earlier studies

Fig. 13 presents a comparison of 50-s attenuation maps derived in this study with the previously published results of DE06 and Ma *et al.* (2016). DE06 used a degree-20 phase-velocity map and GCRA to account for focusing effects, and Ma *et al.* (2016) used finite-frequency kernels. The three independent attenuation studies utilized three independent data sets of Rayleigh wave amplitudes and accounted for focusing effects using three independently derived sets of phase-velocity maps. We use a spherical-harmonic expansion of all maps to degree 12 for these comparisons. Fig. 14 shows the correlation coefficient at each spherical-harmonic degree between the earlier studies and the three attenuation maps from this study for which focusing effects are predicted with degree-20 phase-velocity maps.

At 50 s, agreement between the three maps from this study and the two earlier studies is generally good, and differences between the six comparisons are minor. The cumulative correlation coefficient at degree 12 between the two earlier studies and the map from this study with focusing effects predicted using FFT is slightly lower (approximately 0.80) than when the comparison is performed using

maps from this study with focusing effects predicted using ERT and GCRA (approximately 0.86). At 100 s, the comparison shows good agreement between the maps of this study and Ma *et al.* (2016). At degrees 5–10 the correlation coefficients between this study and DE06 are significantly lower, resulting in smaller cumulative correlation coefficients at degree 12 for the comparison to DE06 (approximately 0.65) than to Ma *et al.* (2016) (approximately 0.65).

We further scrutinize the differences between DE06 and the corresponding result from this study (e.g. Fig. 6a), since we have access to both data sets of amplitude measurements. We consider two possible explanations for the differences between the maps. One, the data used in this study are from a different data set than was utilized by DE06 (Fig. 1). This affects not only the nature of the measurements themselves but also the size (and path coverage) of the data set, which is much larger in the current study. DE06 used 16 225 50-s amplitude measurements and 16 059 100-s amplitude measurements; for comparison, our maps are determined from 390 360 and 393 464 amplitude measurements at 50 and 100 s, respectively. Two, in DE06 the phase-velocity maps and attenuation maps were simultaneously determined from joint inversion of the phase and amplitude data; here focusing effects are predicted and removed from the data prior to inversion.

We investigate if the size of the data set is responsible for the differences. We identify the paths that the two data sets have in

common (e.g. Fig. 1) and invert them separately for 2-D attenuation maps. Focusing effects are predicted using GCRA applied to three sets of phase-velocity maps: the degree-20 and degree-40 maps from this study and the degree-20 maps used by DE06. The un-damped attenuation maps for 50 s are shown in Fig. S14. The attenuation maps from the two different data sets are nearly identical, with correlation coefficients equal to 0.98 for all three pairs of maps. The results for 100 s, which are not shown, are similar to those for 50 s. We therefore conclude that the differences in the measurement techniques and the way focusing effects are removed have little influence on the disagreement between our attenuation maps and DE06. Instead our test suggests that the differences are due to the difference in path coverage of these two studies.

The comparisons described in this section highlight an important result: degree-12 global attenuation maps determined by different groups using independent amplitude data sets and phase-velocity maps exhibit a high level of consistency that did not exist for the previous generation of attenuation studies. Perhaps this finding is not entirely surprising, since all three studies utilized a similar approach for the treatment of source, receiver, and focusing effects. However, it is encouraging to see that when different groups approach the problem separately and with independent data sets, a consistent result begins to emerge. Furthermore, the work described in the current study helps to quantify the extent to which the specific treatment of focusing effects influences the retrieved attenuation structure. Together these two developments suggest that it may be possible to move beyond degree-12 attenuation maps and consider higher-resolution images. As an example, Fig. S15 shows 50-s attenuation maps from this study and Ma *et al.* (2016) expanded to spherical-harmonic degree 20. The comparison shows good agreement between the two maps, especially for degrees <17 (Fig. S16). These degree-20 maps help to resolve more clearly features such as the division between western and eastern North America and areas of anomalously high attenuation along the Mid-Atlantic Ridge.

7 CONCLUSIONS

We used a new global data set of fundamental-mode Rayleigh wave amplitudes to investigate the influence of elastic focusing on attenuation maps. The amplitudes, which have not been previously utilized for seismic tomography, are compared to an independent data set measured using the approach of Ekström *et al.* (1997). The two data sets compare favorably, and the attenuation maps derived from them are highly similar, especially when identical path coverage is used for the comparison. Phase-velocity maps expanded to spherical-harmonic degree 20 and degree 40 are calculated from Rayleigh wave phase delays and used as input to predict focusing effects. Focusing effects are predicted using three different theoretical approaches for surface-wave propagation: the great-circle ray approximation, exact ray theory, and finite-frequency theory. At 50 s, FFT predicts stronger focusing along many paths than GCRA and ERT for the degree-20 phase-velocity map and then ERT for the degree-40 map. At 100 s, the magnitude of the predicted amplitudes is similar for the degree-20 map and weaker using FFT than GCRA and ERT for the degree-40 map. Amplitudes predicted with the two ray-based theories are more strongly sensitive to the roughness of heterogeneity in the phase-velocity map than amplitudes predicted with FFT are.

The six sets of attenuation maps, determined after removing the six sets of focusing predictions from the observed amplitudes and as part of a joint inversion for attenuation coefficients, source terms,

and receiver terms, contain the same primary features and are highly correlated with each other. This result follows directly from comparison of the predicted focusing effects: although the scatter plots of predicted focusing amplitudes would seem to suggest significant differences between the different approaches, the 2-D histograms show that for most paths the predicted values are actually very similar. The magnitude of the heterogeneity in the attenuation maps, however, can depend on the magnitude of the predicted focusing amplitudes. Attenuation maps at 50 s for which focusing effects were predicted using FFT contain stronger heterogeneity than when focusing effects are predicted using GCRA and ERT, in agreement with the difference in magnitude of the predicted amplitudes for those scenarios. We note that we do not observe a systematic difference in the strength of anelastic heterogeneity when focusing effects are predicted with the degree-20 versus degree-40 phase-velocity maps, even though amplitude anomalies predicted with ray-based approaches and degree-40 maps are larger than the equivalent calculation for degree-20 maps, and we offer the following explanation. Whether propagation through a degree-40 versus degree-20 map will affect predicted amplitude varies from path to path and depends on factors such as which velocity anomalies are encountered along the path and how the path is oriented relative to the velocity anomalies. It is not surprising that such path-dependent differences have little overall impact on the attenuation map. On the other hand, differences in the underlying theory used for an amplitude prediction (e.g. GCRA, ERT, and FFT) are likely to be correlated from path to path and, as such, can change the large-scale features in the attenuation map.

The variance reduction of the amplitude observations depends strongly on the predicted focusing amplitudes. At 50 s, the attenuation coefficients, source terms, and receiver terms that result from the inversion provide the best variance reduction when focusing effects are predicted using the two ray-based approaches and degree-20 phase-velocity maps. Using degree-40 maps with GCRA and ERT weakens the variance reduction by 10–30 per cent. At 100 s, focusing effects predicted with FFT provide the best variance reduction, with little difference for the degree-20 and degree-40 maps. These results suggest that, of the three approximate theories tested, ERT is most useful for predicting focusing effects at shorter periods and FFT is most useful at longer periods. This finding agrees with an earlier comparison of measured and predicted focusing effects using spectral-element synthetic seismograms (Dalton *et al.* 2014).

We compare attenuation maps determined using amplitudes observations corrected for focusing effects and using observations not corrected for focusing effects. The two sets of maps are highly correlated at spherical-harmonic degrees <8 for 50 s and <6 for 100 s. At higher degrees the correlation rapidly degrades, indicating that unmodelled focusing effects corrupt the smaller-scale features in attenuation maps while allowing the large-scale features to be robustly imaged.

Constraints on attenuation in the upper mantle can help to identify the presence of water (Rychert *et al.* 2008) and melt (Yang *et al.* 2007; Abers *et al.* 2014). They can also be used to place bounds on the range of mantle potential temperatures (Dalton *et al.* 2009) and to account for anelastic effects on seismic velocity, yielding more accurate estimates of temperature from wave speed (e.g. Goes & van der Lee 2002). With the exception of studies from subduction zones (Stachnik *et al.* 2004; Rychert *et al.* 2008; Pozgay *et al.* 2009; Abers *et al.* 2014), Rayleigh wave amplitudes are the data set most commonly used to investigate upper-mantle attenuation. Accounting for focusing effects on amplitude remains the primary obstacle to imaging attenuation, limiting the resolution of attenuation models

and the degree of agreement between different attenuation studies. In this paper we have demonstrated the level of uncertainty that may be introduced into attenuation models as a result of choices about how best to treat focusing effects. We have also shown good agreement between attenuation maps obtained from inversions of three independent amplitude data sets. The general consistency between the different sets of attenuation maps represents significant progress in global attenuation imaging. This success suggests that it may be worthwhile to try to resolve smaller-scale attenuation features from Rayleigh wave amplitudes.

ACKNOWLEDGEMENTS

We thank editor Xiaofei Chen, Dr Kaiqing Yuan, and an anonymous reviewer for their careful and constructive comments. Thank Göran Ekström for having the GDM52 model available at <http://www.ideo.columbia.edu/~ekstrom/Projects/SWP/GDM52.html>. We are grateful to Zhitu Ma for sharing data and results. The Generic Mapping Tools (GMT) is used to make figures. This work was supported by National Science Foundation award EAR-0944148 to C.A.D.

REFERENCES

- Abers, G.A., Fischer, K.M., Hirth, G., Wiens, D.A., Plank, T., Holtzman, B.K., McCarthy, C. & Gazel, E., 2014. Reconciling mantle attenuation-temperature relationships from seismology, petrology, and laboratory measurements, *Geochem. Geophys. Geosyst.*, **15**, 3521–3542.
- Bhattacharyya, J., Masters, G. & Shearer, P., 1996. Global lateral variations of shear wave attenuation in the upper mantle, *J. geophys. Res.*, **101**, 22 273–22 289.
- Cooper, R.F., 2002. Seismic wave attenuation: energy dissipation in viscoelastic crystalline solids, *Rev. Mineral. Geochem.*, **51**, 253–290.
- Dahlen, F.A. & Tromp, J., 1998. *Theoretical Global Seismology*, Princeton Univ. Press.
- Dalton, C.A. & Ekström, G., 2006a. Global models of surface wave attenuation, *J. geophys. Res.*, **111**, B05317, doi:10.1029/2005JB003997.
- Dalton, C.A. & Ekström, G., 2006b. Constraints on global maps of phase velocity from surface-wave amplitudes, *Geophys. J. Int.*, **167**, 820–826.
- Dalton, C.A. & Faul, U.H., 2010. The oceanic and cratonic upper mantle: clues from joint interpretation of global velocity and attenuation models, *Lithos*, **120**, 160–172.
- Dalton, C.A., Ekström, G. & Dziewonski, A.M., 2008. The global attenuation structure of the upper mantle, *J. geophys. Res.*, **113**, B09303, doi:10.1029/2007JB005429.
- Dalton, C.A., Ekström, G. & Dziewonski, A.M., 2009. Global seismological shear velocity and attenuation: a comparison with experimental observations, *Earth planet. Sci. Lett.*, **284**, 65–75.
- Dalton, C.A., Hjörleifsdóttir, V. & Ekström, G., 2014. A comparison of approaches to the prediction of surface-wave amplitude, *Geophys. J. Int.*, **196**, 386–404.
- Dziewonski, A.M. & Anderson, D.L., 1981. Preliminary reference Earth model, *Phys. Earth planet. Inter.*, **25**, 297–356.
- Ekström, G., 2011. A global model of Love and Rayleigh surface wave dispersion and anisotropy, 25–250 s, *Geophys. J. Int.*, **187**, 1668–1686.
- Ekström, G., Tromp, J. & Larson, E.W.F., 1997. Measurements and global models of surface wave propagation, *J. geophys. Res.*, **102**, 8137–8157.
- Ekström, G., Nettles, M. & Dziewonski, A.M., 2012. The global CMT project 2004–2010: centroid-moment tensors for 13 017 earthquakes, *Phys. Earth planet. Inter.*, **200–201**, 1–9.
- Faul, U.H. & Jackson, I., 2005. The seismological signature of temperature and grain size variations in the upper mantle, *Earth planet. Sci. Lett.*, **234**, 119–134.
- Ferreira, A.M.G. & Woodhouse, J.H., 2007. Source, path and receiver effects on seismic surface waves, *Geophys. J. Int.*, **168**(1), 109–132.
- French, S.W. & Romanowicz, B.A., 2014. Whole-mantle radially anisotropic shear velocity structure from spectral-element waveform tomography, *Geophys. J. Int.*, **199**, 1303–1327.
- Goes, S. & van der Lee, S., 2002. Thermal structure of the North American uppermost mantle inferred from seismic tomography, *J. geophys. Res.*, **107**(B3), doi:10.1029/2000JB000049.
- Gung, Y. & Romanowicz, B., 2004. Q tomography of the upper mantle using three-component long-period waveforms, *Geophys. J. Int.*, **157**, 813–830.
- Jackson, I., FitzGerald, J.D., Faul, U.H. & Tan, B.H., 2002. Grain-size-sensitive seismic wave attenuation in polycrystalline olivine, *J. geophys. Res.*, **107**(B12), 2360, doi:10.1029/2011JB001225.
- Karato, S., 1993. Importance of anelasticity in the interpretation of seismic tomography, *Geophys. Res. Lett.*, **20**, 1623–1626.
- Kustowski, B., Ekström, G. & Dziewonski, A.M., 2008. Anisotropic shear-wave velocity structure of the Earth's mantle, *J. geophys. Res.*, **113**, B06306, doi:10.1029/2007JB005169.
- Larson, E.W.F., Tromp, J. & Ekström, G., 1998. Effects of slight anisotropy on surface waves, *Geophys. J. Int.*, **132**, 654–666.
- Lekić, V., Matas, J., Panning, M. & Romanowicz, B., 2009. Measurement and implications of frequency dependence of attenuation, *Earth planet. Sci. Lett.*, **282**, 285–293.
- Liu, H.P., Anderson, D.L. & Kanomori, H., 1976. Velocity dispersion due to anelasticity: implications for seismology and mantle composition, *Geophys. J. R. astr. Soc.*, **47**, 41–58.
- Ma, Z., Masters, G. & Mancinelli, N., 2016. Two-dimensional global Rayleigh wave attenuation model by accounting for finite-frequency focusing and defocusing effect, *Geophys. J. Int.*, **204**, 631–649.
- Pozgay, S.H., Wiens, D.A., Conder, J.A., Shiobara, H. & Sugioka, H., 2009. Seismic attenuation tomography of the Mariana subduction system: implications for thermal structure, volatile distribution, and slow spreading dynamics, *Geochem. Geophys. Geosyst.*, **10**, Q04X05, doi:10.1029/2008GC002313.
- Reid, F.J.L., Woodhouse, J.H. & van Heijst, H.J., 2001. Upper mantle attenuation and velocity structure from measurements of differential S phases, *Geophys. J. Int.*, **145**, 615–630.
- Ritsema, J., van Heijst, H.J. & Woodhouse, J.H., 2004. Global transition zone tomography, *J. geophys. Res.*, **109**, B02302, doi:10.1029/2003JB002610.
- Ritsema, J., Deuss, A., van Heijst, H.J. & Woodhouse, J.H., 2011. S40RTS: a degree-40 shear-velocity model for the mantle from new Rayleigh wave dispersion, teleseismic traveltime and normal-mode splitting function measurements, *Geophys. J. Int.*, **184**, 1223–1236.
- Romanowicz, B., 1995. A global tomographic model of shear attenuation in the upper mantle, *J. geophys. Res.*, **100**, 12 375–12 394.
- Roth, E.G., Wiens, D.A. & Zhao, D., 2000. An empirical relationship between seismic attenuation and velocity anomalies in the upper mantle, *Geophys. Res. Lett.*, **27**, 601–604.
- Rychert, C.A., Fischer, K.M., Abers, G.A., Plank, T., Syracuse, E., Protti, J.M., Gonzalez, V. & Strauch, W., 2008. Strong along-arc variations in attenuation in the mantle wedge beneath Costa Rica and Nicaragua, *Geochem. Geophys. Geosyst.*, **9**, Q10S10, doi:10.1029/2008GC002040.
- Schaeffer, A.J. & Lebedev, S., 2013. Global shear-speed structure of the upper mantle and transition zone, *Geophys. J. Int.*, **194**, 417–449.
- Selby, N.D. & Woodhouse, J.H., 2002. The Q structure of the upper mantle: constraints from Rayleigh wave amplitudes, *J. geophys. Res.*, **107**, 2097, doi:10.1029/2001JB000257.
- Stachnik, J.C., Abers, G.A. & Christensen, D.H., 2004. Seismic attenuation and mantle wedge temperatures in the Alaska subduction zone, *J. geophys. Res.*, **109**, B10304, doi:10.1029/2004JB003018.
- Trampert, J. & van Heijst, H.J., 2002. Global azimuthal anisotropy in the transition zone, *Science*, **296**, 1297–1299.
- Van Heijst, H.J. & Woodhouse, J.H., 1997. Measuring surface-wave overtone phase velocities using a mode branch stripping technique, *Geophys. J. Int.*, **131**, 209–230.
- Van Heijst, H.J. & Woodhouse, J.H., 1999. Global high-resolution phase velocity distributions of overtone and fundamental-mode surface waves determined by mode branch stripping, *Geophys. J. Int.*, **137**, 601–620.
- Wang, Z. & Dahlen, F.A., 1994. JWKB surface-wave seismograms on a laterally heterogeneous earth, *Geophys. J. Int.*, **119**, 381–401.

- Wang, Z. & Dahlen, F.A., 1995. Validity of surface-wave ray theory on a laterally heterogeneous earth, *Geophys. J. Int.*, **123**, 757–773.
- Woodhouse, J.H. & Wong, Y.K., 1986. Amplitude, phase and path anomalies of mantle waves, *Geophys. J. R. astr. Soc.*, **87**, 753–773.
- Yang, Y., Forsyth, D.W. & Weerantne, D.S., 2007. Seismic attenuation near the East Pacific Rise and the origin of the low-velocity zone, *Earth planet. Sci. Lett.*, **258**, 260–268.
- Zhou, Y., Dahlen, F.A. & Nolet, G., 2004. Three-dimensional sensitivity kernels for surface wave observables, *Geophys. J. Int.*, **158**, 142–168.

SUPPORTING INFORMATION

Additional Supporting Information may be found in the online version of this paper:

Table S1. Summary of data used in this study.

Table S2. Summary of cumulative correlation coefficients at spherical-harmonic degree-12 between each pair of maps of 50 s in Fig. 6.

Table S3. Summary of cumulative correlation coefficient at spherical-harmonic degree-12 between each pair of maps of 100 s in Fig. S5.

Figure S1. Same as in Fig. 3 but for degree-20 phase velocity map of 100 s period.

Figure S2. Same as in Fig. 3 but for degree-40 phase velocity map of 100 s period.

Figure S3. Same as in Fig. 5 but for 100 s.

Figure S4. Comparison of degree-12 50-s attenuation maps obtained when (a) focusing is accounted for during the inversion by jointly inverting for phase-velocity and attenuation maps (e.g. DE06), and (b) focusing is accounted for prior to the inversion by predicting and subtracting focusing effects with GCRA and a degree-20 phase velocity map. No smoothing is applied to these maps, and source and receiver terms are also determined.

Figure S5. Same as in Fig. 6 but for period = 100 s.

Figure S6. Demonstration of the differences between the six 50-s attenuation maps in Fig. 6. (a–e) Differences between the maps expressed relative to the ERT degree-20 map. (f) Correlation coefficient, at each spherical-harmonic degree, between the 50-s ERT degree-20 map and the five other maps in Fig. 6.

Figure S7. Demonstration of the differences between the six 100-s attenuation maps in Fig. S5. (a–e) Differences between the maps expressed relative to the FFT degree-40 map. (f) Correlation

coefficient, at each spherical-harmonic degree, between the 100-s FFT degree-40 map and the five other maps in Fig. S5.

Figure S8. Source and receiver terms at 50 s from the inversion of degree-12 attenuation map for focusing predicted with ERT and degree-40 phase velocity map. (a) and (b) show the $\ln A^S$ and $\ln A^R$ map, respectively. (c) and (d) are histograms showing the distribution of $\ln A^S$ and $\ln A^R$, respectively.

Figure S9. Power spectra of maps in Fig. 6 (50 s) and Fig. S5 (100 s). Blue, red, and black lines denote GCRA, ERT, and FFT, respectively. Solid and dashed lines denote the phase velocity map of degree-20 and degree-40, respectively.

Figure S10. Same as in Fig. 8 but for 100 s.

Figure S11. Same as in Fig. 9 but for 100 s by showing the difference map in Fig. S10.

Figure S12. Same as in Fig. 10 but for 100 s.

Figure S13. Correlation coefficient at each spherical-harmonic degree between Figs S10(d) and S12.

Figure S14. 50-s attenuation maps, with no damping applied, derived using the subset of amplitude measurements held in common by (left) DE06 and (middle) this study. Focusing effects are predicted using GCRA and three different phase-velocity maps—the degree-20 map determined by DE06, the degree-20 map determined in this study, and the degree-40 map determined in this study. Right-hand panel shows the difference between the two sets of map. The difference maps are determined by subtracting the map of this study from the map of DE06. Colour scale shows perturbation in attenuation, dQ^{-1} .

Figure S15. Degree-20 attenuation maps for 50-s Rayleigh waves. (a) From this study, with focusing effects predicted using GCRA and the degree-20 phase-velocity map. (b) The map of Ma *et al.* (2016) is shown here expanded in spherical harmonics to degree 20.

Figure S16. Correlation coefficient at each spherical-harmonic degree between the degree-20 expansion of the 50-s attenuation map of Ma *et al.* (2016) and the six degree-20 maps developed in this study.

(<http://gji.oxfordjournals.org/lookup/suppl/doi:10.1093/gji/ggw322/-/DC1>).

Please note: Oxford University Press is not responsible for the content or functionality of any supporting materials supplied by the authors. Any queries (other than missing material) should be directed to the corresponding author for the paper.